Radial Distribution Function Imaging by STEM Diffraction: phase mapping and analysis of heterogeneous nanostructured glasses

Xiaoke Mu[1,2], Di Wang[1,3], Tao Feng[4] and Christian Kübel[1,2,3]

[1.] Institute of Nanotechnology (INT), Karlsruhe Institute of Technology (KIT), 76344 Eggenstein-Leopoldshafen, Germany
[2.] Helmholtz-Institute Ulm for Electrochemical Energy Storage (HIU), Karlsruhe Institute of Technology (KIT), 89081 Ulm, Germany
[3.] Karlsruhe Nano Micro Facility (KNMF), Karlsruhe Institute of Technology (KIT), 76344 Eggenstein-Leopoldshafen, Germany
[4.] Herbert Gleiter Institute of Nanoscience, Nanjing University of Science and Technology (NJUST), 210094 Nanjing, China

Abstract

To overcome some of the challenges in characterizing heterogeneous nanostructured amorphous materials, we developed a new TEM method, RDF imaging, combining scanning transmission electron microscopy diffraction mapping with radial distribution function (RDF) analysis followed by hyperspectral analysis, to enable phase analysis and mapping of heterogeneous amorphous structures purely based on their short- and medium range atomic order. We applied this method to an amorphous zirconium oxide and zirconium iron multilayer system, demonstrating an extreme sensitivity of the method to small atomic packing variations. This approach has great potential to understand local structure variations in glassy composite materials and to provide new insights to correlate structure and properties of glasses.

1. Introduction

Analyzing the atomic structure of amorphous materials has challenged materials scientist for a long time because of their disordered atomic arrangement. Only few experimental means offer ways to characterize these disordered structures. The atomic radial distribution function (RDF) describes the probability to find certain atomic pairs as a function of the pair separation and consequently, provides short and medium range structural information. Therefore, it is one of the most important tools for structural characterization of amorphous materials. The RDF can be determined from X-ray and neutron diffraction data [1][2] and has been widely applied to investigate amorphous materials such as organic solids [3], liquids [4][5], metallic glasses [6], phase-change memory materials [7] and nano-scaled energy storage materials [8][9]. Jacques et al. combined RDF analysis with X-ray diffraction computed tomography (XRD-CT) [10] for spatially resolved RDF analysis of heterogeneous structures, where structural features around tens of micrometers could be resolved [11].

The spatial resolution can be improved further by utilization electron diffraction techniques in a transmission electron microscope (TEM), where RDF measurements sampling an area of hundreds nanometer can be easily achieved by selected area electron diffraction (SAED) [12][13]. However, SAED still averages relatively large sample areas and hides plenty of information in the averaged signal. Especially, in case of heterogeneous nanostructured materials this averaging is critical. Due to the required high resolution in the diffraction pattern, it is not straightforward to take RDFs from further reduced sampling volumes. Pioneering work for RDF analysis of nano scale volumes was done by McBride et al. [14] using convergent beam electron diffraction followed by a deconvolution procedure. Nevertheless, RDFs obtained by single or few independent point measurements without a systematic statistical analysis of the different sampling areas are far from satisfactory to understand the

structure of heterogeneous amorphous materials, especially if only limited preliminary knowledge of their complex phase distribution is available, e.g. as in nanoglasses. The desire to explain their unusual structures and properties [15][16][17] requires improved characterization methods.

Fluctuation electron microscopy (FEM) [25] combining quasi-parallel illumination with a nanosized beam in scanning transmission electron microscopy (STEM) measures statistical variations in diffraction patterns taken from different sample areas. FEM analysis reveals heterogeneities of the atomic structure and establishes the medium-range atomic order in amorphous materials [18][19]. It has been applied e.g. for the local analysis of shear bands in metallic glasses [20][21]. However, the interpretation of the abstract diffraction variations is not straightforward and usually requires supplementary simulations, such as reverse Monte Carlo modeling [22].

A description of amorphous materials based on their direct interatomic distances, as depicted by RDF analysis of the short- and medium-range order, is more intuitive. Therefore, with this work, we introduce a new TEM method: STEM RDF mapping to characterize heterogeneous nanostructured amorphous materials and composites. Using a quasi-parallel nano electron diffraction setup [23][24], where diffraction patterns from nano volumes can be acquired with high angular resolution, we combine RDF analysis with STEM diffraction mapping [26] (D-STEM) with a spatial resolution of ~1 nm. These RDF maps can be analyzed by hyperspectral statistical analysis such as multiple linear least square (MLLS) fitting to construct the phase distribution within a heterogeneous amorphous material purely based on the short- and medium-range order of the different glass phases. In addition, by analyzing the MLLS fitting and the RDFs more in details, it is possible to characterize and understand the structure of the clusters in the different phases. To illustrate the potential of this approach, we applied this new method to an amorphous zirconium oxide (ZrO_2) and zirconium iron ($Zr_{0.2}Fe_{0.8}$) multilayer system, which demonstrated that the method is extremely sensitive even to small atomic packing variations. This approach has great potential to understand nanoscale structural variations in glasses, glass composites and shear bands to provide new insights to correlate structure and properties of glasses, e.g. to understand their mechanical or thermal behavior.

2. Method description: experimental settings and data analysis procedures

Figure 1 schematically illustrates the procedure for data acquisition and analysis to obtain amorphous structure distribution maps. A STEM setup with quasi-parallel nano beam illumination providing a nano-sized probe with a small semi-convergence angle (typically < 1 mrad) is used for the experiments. The small convergence angle does not significantly degrade the angular resolution of the diffraction patterns as can be seen from a representative diffraction pattern in figure 1b. Therefore, the RDFs can be directly computed from the diffraction patterns acquired with nano beam illumination without deconvolution with the beam spread function (a function depicting the center disc of the diffraction pattern formed by the unscattered electrons) as described in [14]. An array of diffraction patterns is recorded by stepwise scanning the beam across a predefined area of interest (D-STEM). The recorded diffraction patterns have to include high scattering angles, where the high frequency structural information required for the RDF analysis is encoded. Taking advantage of the strong interaction of electrons and matter, electron diffraction provides a strong signal even at high diffraction angles with reasonable acquisition times/dose. This enables fast scanning during D-STEM acquisition.
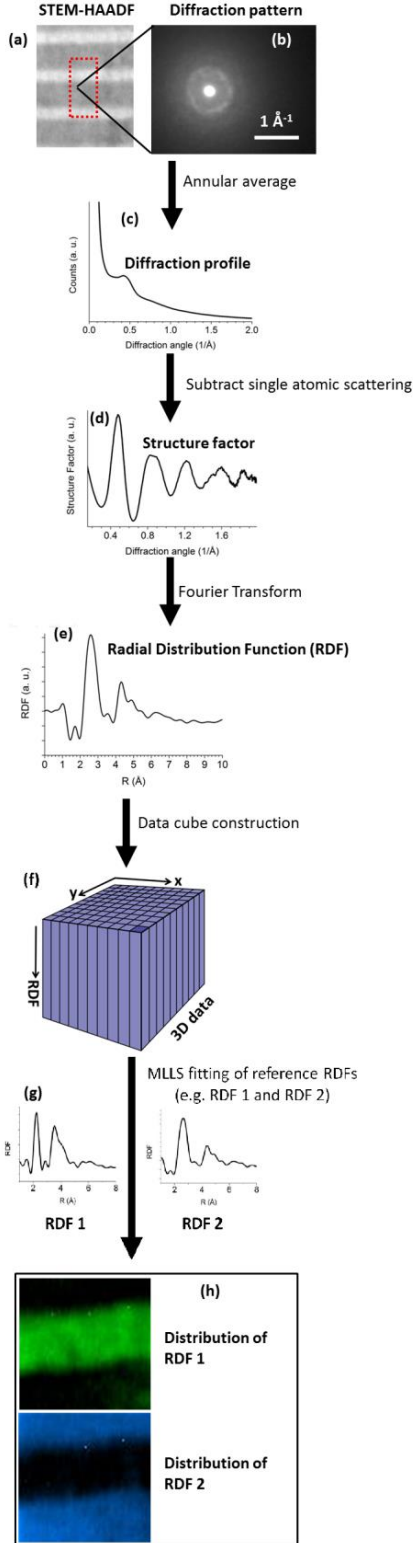
STEM-HAADF **Diffraction pattern**

(a)

(b)

1 Å⁻¹

Annular average

(c) Diffraction profile

Subtract single atomic scattering

(d) Structure factor

Fourier Transform

(e) Radial Distribution Function (RDF)

Data cube construction

(f)

RDF

3D data

MLLS fitting of reference RDFs
(e.g. RDF 1 and RDF 2)

(g)

RDF 1   RDF 2

(h)

Distribution of RDF 1

Distribution of RDF 2

Figure 1 (c to e) schematically describes the procedure to compute the RDF from the experimental diffraction patterns. Details with the theoretical background for RDF extraction from diffraction patterns are given in [12][13]. In the current work, the diffraction patterns were integrated azimuthally to obtain radius profiles $I(s)$ (figure 1c), where s = 2θ/λ, θ is half of the scattering angle and λ the incident wavelength. The azimuthal integration is necessary, not only to increase the signal to noise ratio at large scattering angles, but also to reduce fluctuations of the diffraction profiles at different scanning areas caused by the finite sampling of cluster orientations for small interaction volumes. Depending on the constituent cluster size and the probe diameter, a minimum sample thickness will be needed to obtain a stable diffraction profile. Nevertheless, even with the ~1 nm beam diameter used in this study, typical TEM sample thicknesses were sufficient for reproducible diffraction profiles.

Figure 1 Sketch of the procedure to calculate the RDF distribution map from experimental D-STEM data: (a) HAADF-STEM image with the area for D-STEM acquisition outlined. (b) Parallel nano beam diffraction pattern acquired in D-STEM. (c) Annular averaged diffraction profile. (d) Structure factor deduced by subtraction and normalization with single atomic scattering factors. (e) RDF obtained by Fourier transform of the structure factor. (f) Sketch of the constructed 3D RDF cube. (g) Reference RDFs obtained from selected areas of the data set. (h) Structure maps obtained by MLLS fitting of RDF 1 and 2 to the RDF cube.

The structure factors (figure 1d) are calculated by subtracting and normalizing with single atomic scattering factors, as describe in equation (1)

$$\varphi(s) = \frac{I(s) - N\langle f(s)^2\rangle}{N\langle f(s)\rangle^2} s \qquad (1),$$

where N is the number of atoms within the volume sampled by the electron probe, $f(s)$ are the parameterized elemental scattering factors, calculated based on [27]. $\langle f(s)\rangle = \sum_i C_i f_i(s)$ denotes an average of elemental atomic scattering factor $f_i(s)$ over all elements i present in the material weighted by their atomic percentages C_i.

The RDFs ($G(r)$) are obtained by a sine Fourier transformation of the structure factors according to equation (2)

$$G(r) = \int_0^{S_{max}} \varphi(s)\sin(2\pi sr)ds \qquad (2).$$

The only adjustable parameter in the RDF calculation is N, which is determined for each RDF in the map by minimizing $\varphi(s)$ in equation (1) to approach zero at large scattering angles (s). This reduces effects caused by mass (thickness × atomic density) from the diffraction data and makes the RDF analysis robust dealing with voids and thickness variations. However, $\langle f(s)\rangle$ is only a coarse approximation for multi-element materials [28]. Together with multiple and inelastic scattering contributing to the diffraction patterns, the diffraction profiles cannot be fitted well by the averaged scattering factor both at low and high angles simultaneously, hence resulting in low-frequency artefacts, which do not correspond to the real structure of the sample [28][29]. Following the

procedure outlined in [28], the low-frequency artefacts are eliminated by fitting and subtracting a smooth 4th-order polynomial function from the structure factor calculated from equation (1). This approach is robust for background subtraction to calculate the structure factor.

The diffraction patterns in the experimental image arraywere each individually processed as discussed above to construct the 3D RDF data cube. The RDF cube can be analyzed using hyperspectral techniques, for example by MLLS. MLLS fits the data cube with linear combinations of reference spectra , thus reduces the dimension of the cube to 2D images of the respective fitting coefficients for the corresponding reference spectra. It has been implemented in DigitalMicrograph^{TM} (DM) as a standard plugin [30]. The reference spectra can be obtained either by measuring the pure phases or from the RDF matrix itself, for example by multivariate statistical analysis (MSA) [31]. The 2D RDF images (phase images) correspond to the atomic packing encoded in the RDFs, thus a structural phase map is obtained. The results can also be correlated with simultaneously acquired energy dispersive X-ray spectroscopy (EDX) maps or with electron energy-loss spectroscopy (EELS) maps for further comprehensive compositional investigations.

3. Application to amorphous ZrFe/ZrO₂ multilayers

We applied the method described above to an amorphous ZrO_2 and $Zr_{0.2}Fe_{0.8}$ (ZrFe) multilayer (ZO/ZF) system. The amorphous multilayer structure has been prepared by magnetron sputtering with separate ZO and ZF targets. A cross-section of the ZO/ZF multilayer sample was prepared for TEM analysis by focused ion beam (FIB, ZEISS AURIGA) milling and further thinned by low-voltage argon ion milling (Fischione Nanomill 1040) at 700 eV beam energy for 40 min. followed by fine milling at 500 eV for 35 min. The final sample thickness is around 0.4 inelastic mean free path (MFP) determined by low-loss EELS analysis, corresponding to ~50 nm sample thickness based on the average MFP calculated using Mitchell's DM plugin "mean free path estimator" [32].

The initial characterization of the multilayer structure was performed using an aberration (image) corrected FEI Titan 80-300 operated at 300 kV in STEM mode with spot size 5 and a 70 µm condenser (C2) aperture resulting in a nominal beam diameter smaller than 1 nm. The system is equipped with an EDAX s-UTW detector for EDX analysis and a Gatan Tridium 863 image filter for EELS/EFTEM analysis. For the EELS acquisition, a camera length of 77 mm and a 2.0 mm entrance aperture energy filter were selected with a convergence semi-angle of 14 mrad and collection semi-angle of 10 mrad. The HAADF-STEM image (figure 2a) fits to the expected multilayer structure of ZrO_2 (dark) and ZrFe (bright). The STEM-EELS and EDX elemental maps (figure S 1) confirm the composition variation of the multilayer structure with an average stoichiometry of about Zr:Fe:O = 1:1:2 measured by combining EELS and EDX analysis. The stochimetry at the center of the ZrFe layer is Zr:Fe = 1:4 and at the center of the ZrO_2 layer it is Zr:O = 1:2.

The D-STEM experiments were performed using a Tecnai F20 ST (Philips) operated at 200 kV in µp-STEM mode and equipped with a NanoMegas ASTAR system, which was initially designed for automated crystal orientation mapping (ACOM) [33], e.g. for orientation analysis of nanocrystalline materials [34]. For the data acquisition, spot size 8, gun lens 6, extraction voltage of 3.9kV and a 30 µm C2 aperture were adopted. These settings results in a quasi-parallel beam with a convergent semi-angle of 0.8 mrad and a probe size of approximately 1 nm. The scanning function was controlled by the ASTAR system. Diffraction patterns were recorded by an external camera with a frame size of 580 × 580 pixels. We set the readout frequency of the camera to 50 fps (frames per second, 0.02 s per pattern), and applied a small camera length of 100 mm for the diffraction pattern acquisition. The

maximum recording angle in the current experimental setup is 50.2 mrad corresponding to $s_{max} = 2.0$ $\mathring{A}^{-1}$ in reciprocal space.

The acquired diffraction patterns were exported as 16 bit gray scale TIFF files. These TIFF files were imported into Matlab for RDF calculation. The mean scattering factor was calculated from the parameterized elemental scattering factors [27] using the average composition of the multilayers determined experimentally. To investigate the effect of compositional variations on the fitting, RDFs were calculated with different stoichiometries varying from an average atomic number of 18.7 corresponding to pure ZrO_2 to 28.8 corresponding to pure ZrFe (figure S 2). Both peak positions and shape were negligibly influenced, confirming that we do not add a systematic bias in the RDF mapping by using the average of the single atomic scattering factors. Therefore a mean stoichiometry of Zr:Fe:O = 1:1:2 was used for calculating all RDFs. The RDF cube was calculated following the description in section 2.
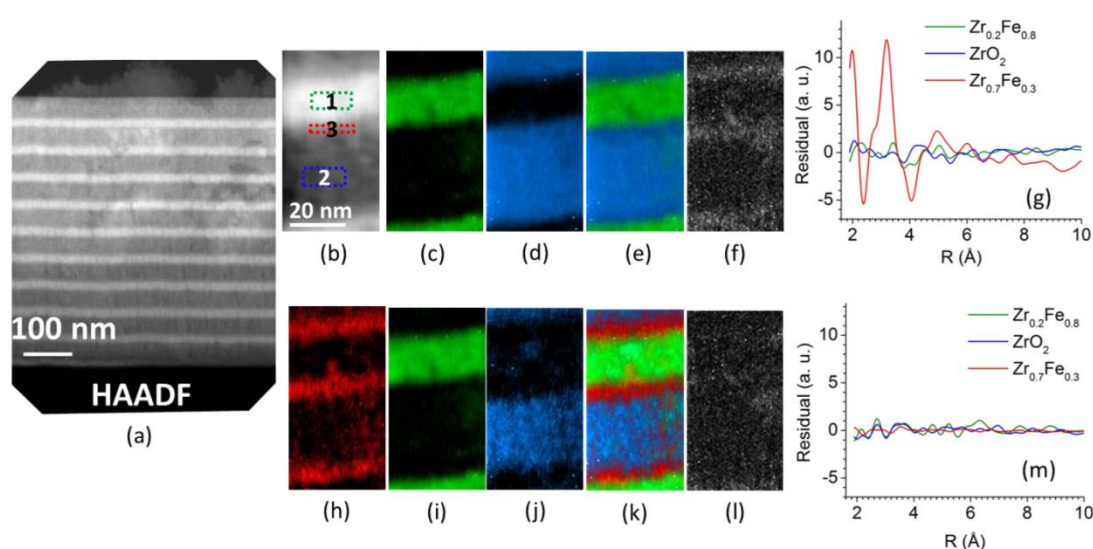

Figure 2 (a) STEM HAADF image of the ZO/ZF multilayer. (b) (Virtual) HAADF image calculated from the D-STEM measurement. Results from MLLS fitting using only the ZrFe and ZrO_2 reference RDFs: Image of the fitting coefficients for (c) the ZrFe reference RDF and (d) the ZrO_2 reference RDF. (e) Superposition of c and d. (f) Map of the fitting error. (g) Residuals taken from the areas indicated by the green, blue and red box in b. Results from MLLS fitting including the interface RDF together with the ZrFe and ZrO_2 reference RDFs: Image of the fitting coefficients for (h) the interface RDF, (i) the ZrFe reference RDF, (j) and the ZrO_2 reference RDF. (k) Superposition of h, i and j. (i) Map of the fitting error. (l) Residuals taken from areas indicated by the green, blue and red box in b.

Figure 2b shows a virtual HAADF image which was calculated from the D-STEM data by applying a virtual dark field aperture selecting high angle signals. It fits well to the STEM-HAADF image shown in figure 1a. MLLS fitting was applied for the RDF cube. The reference RDFs for the amorphous ZrFe and ZrO_2 phases (figure 3a) were obtained by averaging the RDFs from the areas indicated in blue and green in figure 2b. By fitting the two reference RDFs to the RDF cube, the ZrFe and ZrO_2 phase distribution could be easily identified as shown in figure 2c/d. The superposition of the two images provides the phase map (figure 2e), where the phase determination is based only on the atomic structure, the short- and medium-range order of the clusters making up the two glass layers.

The fitting errors, generated during the MLLS processing, described by the cost function χ^2 for fitting a linear combination of the reference RDFs to the experimental RDF cube, can be displayed as an error map (figure 2f). Surprisingly, thin line features with a width of around 3.5 nm are visible in the error map (figure 2f) at the transition between ZrO_2 and ZrFe, which means significant errors in the

phase identification there. This is in contrast to the elemental maps determined by STEM-EELS and -EDX analysis (figure S 1), which do not indicate an additional phase present in this interface region. By subtracting the fitting functions (the linear combinations of the ZrFe RDF and ZrO_2 RDF references) from the RDF cube, a residue functions can be obtained. Figure 2g shows the residuals determined for the three regions indicated in Figure 2b. The red residual curve is integrated from the interfacial area between the ZrFe and ZrO_2, corresponding to the location with the bright features in the error map (figure 2f). It exhibits non-negligible errors significantly larger than the other two residuals within the layers. This means that the RDF in the interfacial area cannot be explained by a simple superposition of the two references for ZrFe and ZrO_2. Consequently, this means that the observed features between the ZrFe and ZrO_2 layers in the error map correspond to an interfacial layer with an atomic structure different from both the amorphous ZrFe and the ZrO_2 layer. This is crucial information not visible in the simple STEM-EELS/EDX measurements.

The RDF of the interfacial layer (interface RDF) was extracted from the area indicated in red in figure 2b, where the significant fitting errors in the error map (figure 2f) have been observed. The interface RDF is shown in red in figure 3a. It exhibits very similar features as the ZrO_2 RDF (figure 3a, blue curve), but a small shift of the first and second pronounced peaks is observed, which can be attributed to slightly reduced atomic distances. The observed shift is 0.04 Å for the first peak (highlighted in the enlarged part of the RDF in figure 3b) and 0.06 Å for the second peak. The precision for RDF analysis has been reported to be 0.02 Å in various experiments [12][28]. The precision should be even better in the current case, as the RDF cube is obtained by D-STEM with all experimental settings of the data acquisition at each pixel identical. Therefore, the observed peak shifts for the interface RDF are reliable.
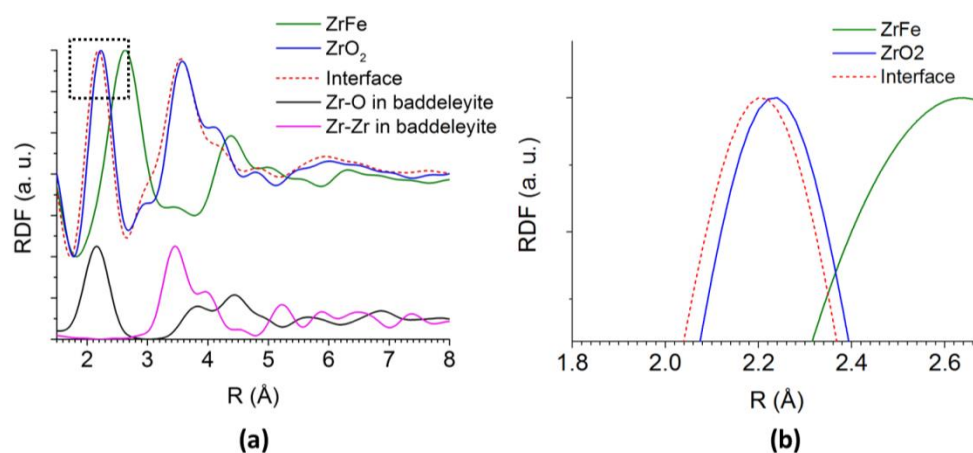
Figure 3 (a) RDFs taken from the amorphous ZrFe (green), ZrO_2 (blue), and interfacial layers (red dashed) as indicated in Figure 2b with the calculated Z-O (black) and Zr-Zr (pink) partial RDFs based on the monoclinic crystalline baddeleyite ZrO_2. (b) Enlarged view of the first peak in **a** showing the shift of the first peak of the interface RDF compared to the ZrO_2 RDF.

Another MLLS fitting was performed with the interface RDF included in addition to the ZrFe and ZrO_2 RDF. Figures 2h-2j show the images of the new fitting coefficients corresponding to the interface, the ZrFe and the ZrO_2 RDF. The corresponding new phase map (figure 2k) was obtained by superposition of the three coefficient images. The interface layer between ZrFe and ZrO_2 layers can be clearly seen. Moreover, the new error map (figure 2l) shows vanishing features compared to the error map (figure 2f) based on only fitting the ZrFe and ZrO_2 RDF. Furthermore, all three RDF residuals were successfully reduced to a similar low level. This further proves the reliability for identifying the interfacial layer and its RDF.

In order to understand the atomic structure of the interfacial layers, partial RDFs for ZrO_2 (figure 3a) based on the monoclinic crystalline baddeleyite structure [35] were calculated as described in [36]. Kinematic element specific partial diffraction profiles were calculated based on a baddeleyite supercell with 168 atoms. The diffraction intensities were damped at high angles applied to mimic the amorphous behavior. Partial RDFs were calculated from the simulated diffraction data analogous to the experimental RDFs. In figure 3a, the black curve corresponds to the Zr-O pair distribution and the pink to Zr-Zr pair distribution. The O atoms only have a small contribution to the diffraction intensity compared to the Fe and Zr atoms because of the scattering cross-section decreasing with a power of 2 with decreasing atomic number, therefore partial RDFs for O-O pairs are not shown here. Comparing the simulated partial RDFs to the experimental ZrO_2 RDF, one can conclude that the first pronounced peak in the experimental ZrO_2 RDF corresponds to the average Zr-O bonding distance. The second pronounced peak can mainly be attributed to Zr-Zr pairs. The good agreement between the experimental and the calculated RDFs confirms that the short-range order of the clusters constituting the ZrO_2 glass is similar to baddeleyite with about 2.8% increased average distances. The small peak shift of the interface RDF can be explained by Fe atoms replacing the Zr atoms in the ZrO_2 clusters. As Fe has a smaller atomic radius compared to Zr, replacing Zr by Fe in the interface layer reduces the average bonding distance between O and Zr/Fe (the first pronounced peak) as well as between Zr/Fe to Zr/Fe (the second pronounced peak) and hence generates the unique interfacial layer between the amorphous ZrFe and ZrO_2. It is worthwhile to note that the local atomic packing in this ZrFeO interfacial layer is the same as the atomic packing in the ZrO_2 layer. The presence of Fe in the interface layer is also confirmed by EELS Fe-L edge analysis, which results in an approximate average amount of Fe atoms in the interface area of 20% compared to the middle of the ZrFe layers. EDX analysis indicates an average composition of Zr:Fe ≈ 7:3 in the interfacial region. While this analysis does not provide a conclusive mechanistic explanation how Fe has replaced Zr, the RDF mapping clearly confirms the formation of a defined interface phase and enabled its direct structural analysis, whereas EELS/EDX analysis by itself could not be interpreted unambiguously.

The results of RDF imaging of the ZF/ZO amorphous multilayers show that the new method is highly sensitive to short-range order, i.e. atomic packing. The detection of the thin interface layer is a great example of the sensitivity of the RDF analysis using the information encoded in the total diffraction signal. More crucially, this sensitivity is further enhanced by the systematic analysis of the RDF cube using MLLS fitting, which cannot be realized by traditional individual independent RDF measurements. Moreover, instead of manually selecting RDF references for MLLS fitting, a more sophisticated hyperspectral analysis could include the application of matrix decomposition algorism, such as MSA, in the future for automated feature recognition and component extraction in complex systems.

In principle, the RDFs include information on medium range order (higher order (> 3th) coordination) as peaks at high radius. However, depending on the cluster size, these peaks in the RDF will diminish with increasing radius as the distance approaches the correlation length in the cluster as demonstrated in [10]. Furthermore, because of the limited probe size (~ 1 nm) of the electron beam, which is necessarily small for providing sufficient resolution e.g. to detect the thin interfacial layer, it is not possible to capture the atomic correlations (structural coherence) larger than the probe size. Consequently peaks corresponding to distances larger than around 6 Å, which is the lower boundary for medium range order, are strongly damped in our RDFs. Nevertheless, the information on medium range order can be easily recorded by increasing the probe size, but at the cost of spatial resolution in the corresponding structure maps.

The RDF map taken from the D-STEM experiment realize 2D phase imaging of heterogeneous amorphous materials solely based on structural differences. The contrast mechanism effectively

suppresses disturbances caused by fluctuation of sample thickness and avoids uncertainties distinguishing low-density areas and voids, as present in traditional BF-TEM or STEM-HAADF imaging of amorphous materials. Such an advantage is essential to study e.g. nanoglasses [16] or shear-bands in metallic glasses [20][21]. The method may even be applied to organic solids, such as pharmaceutics, polymers, and organic solar cell as well as to liquids with advanced in-situ TEM setups. It might initiate a way to discover the concealed secretes in nanoscale reactions between amorphous phases.

4. Conclusion

With this work, we introduce a new method for analyzing complex nanostructured glasses: RDF mapping. It utilizes diffraction imaging in scanning transmission electron microscopy (D-STEM) with quasi-parallel nano beam configuration. A 3D RDF cube can be obtained by applying RDF analysis to the hundred thousands of experimental diffraction patterns. 2D phase maps corresponding to the short- and medium-range structural information are obtained. An automated comparison of the RDFs in the RDF cube using hyperspectral analysis approaches, such as MLLS fitting, provides an efficient approach to comprehensively analyze the atomic structure of heterogeneous amorphous materials.

We applied the newly development method to an amorphous $Zr_{0.2}Fe_{0.8}/ZrO_2$ multilayer system. The analysis shows that not only both the ZrO_2 and the ZrFe phases can be unambiguously distinguished based on the arrangement of their atomic packing, but also an interfacial layer between the ZrO_2 and ZrFe layer was identified, which was also represented in STEM-EELS and EDX maps, but could not be unambiguously identified only based on the elemental composition. The atomic structure of the interfacial layers was discovered by comparing the information embedded in the experimental RDF profile with a simple RDF simulation in combination with the chemical information from STEM-EELS/EDX analysis.

We demonstrated the power of this method not only to detect atomic packing variations in nanoscale heterogeneous amorphous materials, but also to interpret the results using the concrete information depicted in the RDF. It opens a route to provide more answers to a plethora of mysteries of amorphous matter.
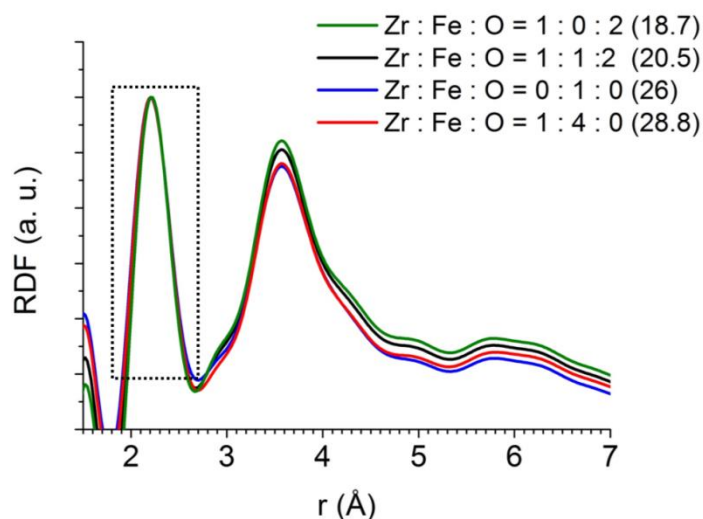
5. Acknowledge

Supplementary information
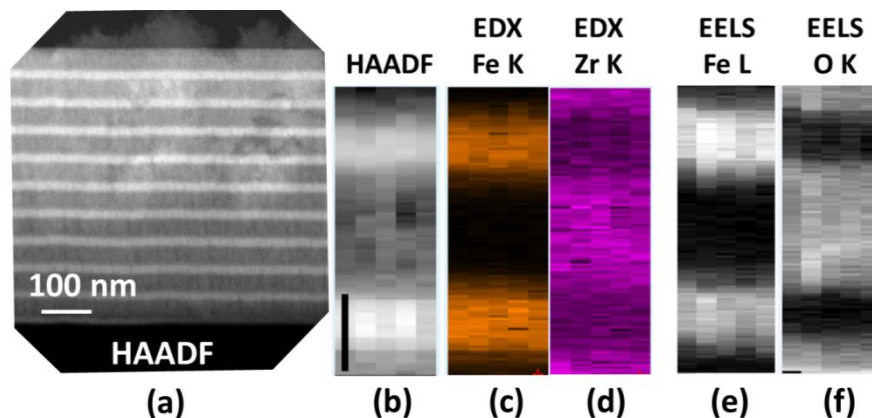
Figure S 1 (a) HAADF overview image of the multilayer structure. (b) HAADF image taken together with the EELS/EDX spectral image. The vertical scale bar is 20 nm. (c) EDX map of Fe-K signal. (d) of Zr-K signal. (e) EELS map of Fe-L, (f) of O-K.

Figure S 2 Test of background subtraction for the RDF calculation with varying atomic ratios. The green, black, blue and red curves are RDFs calculated from diffraction patterns taken from the interfacial region with atomic ratios set to Zr:Fe:O = 1:0:2, 1:1:2 (the setting used in this work), 0:1:0 and 1:4:0 respectively. The numbers in the brackets in the legend are the average atomic numbers. No change in both peak position and peak shape is observed, which is the key information used in MLLS fitting and structure interpretation.

1 References

[1] E. Takeshi and S. J. L. Billinge, "Chapter 3 - The Method of Total Scattering and Atomic Pair Distribution Function Analysis," *Underneath Bragg Peaks Struct. Anal. Complex Mater.*, vol. 16, pp. 55–111, 2012.

[2] T. Proffen and S. Billinge, "Structural analysis of complex materials using the atomic pair distribution function—a practical guide," *Zeitschrift für Krist.*, vol. 218, pp. 132–143, 2003.

[3] J. Waring, R. Lovell, G. Mitchell, and A. Windle, "Radial distribution functions of non-crystalline polymers and their application to the structural analysis of PMMA," *J. Mater. Sci.*, vol. 17, 1982.

[4]   J. G. Kirkwood and E. M. Boggs, "The Radial Distribution Function in Liquids," *J. Chem. Phys.*, vol. 10, no. 6, p. 394, 1942.

[5]   P. Chirawatkul, A. Zeidler, P. S. Salmon, S. Takeda, Y. Kawakita, T. Usuki, and H. E. Fischer, "Structure of eutectic liquids in the Au-Si, Au-Ge, and Ag-Ge binary systems by neutron diffraction," *Phys. Rev. B*, vol. 83, no. 1, p. 014203, Jan. 2011.

[6]   M. Ghafari, S. Kohara, H. Hahn, H. Gleiter, T. Feng, R. Witte, and S. Kamali, "Structural investigations of interfaces in Fe90Sc10 nanoglasses using high-energy x-ray diffraction," *Appl. Phys. Lett.*, vol. 100, no. 13, p. 133111, 2012.

[7]   K. B. Borisenko, Y. Chen, D. J. H. Cockayne, S. A. Song, and H. S. Jeong, "Understanding atomic structures of amorphous C-doped Ge2Sb2Te5 phase-change memory materials," *Acta Mater.*, vol. 59, no. 11, pp. 4335–4342, Jun. 2011.

[8]   N. Yamakawa, M. Jiang, B. Key, and C. P. Grey, "Identifying the local structures formed during lithiation of the conversion material, iron fluoride, in a Li ion battery: a solid-state NMR, X-ray diffraction, and pair distribution function analysis study.," *J. Am. Chem. Soc.*, vol. 131, no. 30, pp. 10525–36, Aug. 2009.

[9]   B. Key, M. Morcrette, J. M. Tarascon, and C. P. Grey, "Pair distribution function analysis and solid state NMR studies of silicon electrodes for lithium ion batteries: understanding the (de)lithiation mechanisms.," *J. Am. Chem. Soc.*, vol. 133, no. 3, pp. 503–12, Jan. 2011.

[10]   S. D. M. Jacques, M. Di Michiel, S. a J. Kimber, X. Yang, R. J. Cernik, A. M. Beale, and S. J. L. Billinge, "Pair distribution function computed tomography.," *Nat. Commun.*, vol. 4, p. 2536, Jan. 2013.

[11]   M. Álvarez-Murga, P. Bleuet, and J.-L. Hodeau, "Diffraction/scattering computed tomography for three-dimensional characterization of multi-phase crystalline and amorphous materials," *J. Appl. Crystallogr.*, vol. 45, no. 6, pp. 1109–1124, Nov. 2012.

[12]   D. J. H. Cockayne, D. R. McKenzie, and C. D.J.H., "Electron Diffraction Analysis of Polycrystalline and Amorphous Thin Films," *Acta Crystallogr. A*, vol. 44, pp. 870–878, 1988.

[13]   D. J. H. Cockayne, "The Study of Nanovolumes of Amorphous Materials Using Electron Scattering," *Annual Review of Materials Research*, vol. 37. pp. 159–187, 2007.

[14]   W. McBride, D. Cockayne, and C. Goringe, "Reduced density function analysis using convergent electron illumination and iterative blind deconvolution," *Ultramicroscopy*, vol. 76, no. 1999, pp. 115–123, 1999.

[15]   R. Witte, T. Feng, J. X. Fang, a. Fischer, M. Ghafari, R. Kruk, R. a. Brand, D. Wang, H. Hahn, and H. Gleiter, "Evidence for enhanced ferromagnetism in an iron-based nanoglass," *Appl. Phys. Lett.*, vol. 103, no. 7, p. 073106, 2013.

[16]   H. Gleiter, "Our thoughts are ours, their ends none of our own: Are there ways to synthesize materials beyond the limitations of today?," *Acta Mater.*, vol. 56, no. 19, pp. 5875–5893, Nov. 2008.

[17]   J. X. Fang, U. Vainio, W. Puff, R. Würschum, X. L. Wang, D. Wang, M. Ghafari, F. Jiang, J. Sun, H. Hahn, and H. Gleiter, "Atomic structure and structural stability of Sc75Fe25 nanoglasses.," *Nano Lett.*, vol. 12, pp. 458–63, 2012.

[18]   M. M. J. Treacy, J. M. Gibson, L. Fan, D. J. Paterson, and I. McNulty, "Fluctuation microscopy: a probe of medium range order," *Reports Prog. Phys.*, vol. 68, no. 12, pp. 2899–2944, Dec. 2005.

[19]   P. M. Voyles and D. A. Muller, "Fluctuation microscopy in the STEM," *Ultramicroscopy*, vol. 93, pp. 147–159, 2002.

[20]   V. Schmidt, H. Rösner, M. Peterlechner, G. Wilde, and P. M. Voyles, "Quantitative Measurement of Density in a Shear Band of Metallic Glass Monitored Along its Propagation Direction.," *Phys. Rev. Lett.*, vol. 115, no. 3, p. 035501, Jul. 2015.

[21]   H. Rösner, M. Peterlechner, C. Kübel, V. Schmidt, and G. Wilde, "Density changes in shear bands of a metallic glass determined by correlative analytical transmission electron microscopy.," *Ultramicroscopy*, vol. 142, pp. 1–9, Jul. 2014.

[22]   M. M. J. Treacy and K. B. Borisenko, "The local structure of amorphous silicon.," *Science*, vol. 335, no. 6071, pp. 950–3, Feb. 2012.

[23]   K. J. Ganesh, M. Kawasaki, J. P. Zhou, and P. J. Ferreira, "M icroscopy M icroanalysis D-STEM : A Parallel Electron Diffraction Technique Applied to Nanomaterials," *Microsc. Microanal.*, vol. 16, pp. 614–621, 2010.

[24]   D. Alloyeau, C. Ricolleau, T. Oikawa, C. Langlois, Y. Le Bouar, and A. Loiseau, "STEM nanodiffraction technique for structural analysis of CoPt nanoparticles," *Ultramicroscopy*, vol. 108, no. 7, pp. 656–62, Jun. 2008.

[25]   F. Yi, P. Tiemeijer, and P. M. Voyles, "Flexible formation of coherent probes on an aberration-corrected STEM with three condensers.," *J. Electron Microsc. (Tokyo).*, vol. 59 Suppl 1, pp. S15–21, Aug. 2010.

[26]   C. Gammer, V. Burak Ozdol, C. H. Liebscher, and A. M. Minor, "Diffraction contrast imaging using virtual apertures," *Ultramicroscopy*, vol. 155, pp. 1–10, Aug. 2015.

[27]   E. J. Kirkland, *Advanced Computing in Electron Microscopy*. 2010, pp. 1–289.

[28]   X. Mu, S. Neelamraju, W. Sigle, C. T. Koch, N. Totò, J. C. Schön, A. Bach, D. Fischer, M. Jansen, and P. a. van Aken, "Evolution of order in amorphous-to-crystalline phase transformation of MgF 2," *J. Appl. Crystallogr.*, vol. 46, no. 4, pp. 1105–1116, Jul. 2013.

[29]   G. Anstis, Z. Liu, and M. Lake, "Investigation of amorphous materials by electron diffraction—The effects of multiple scattering," *Ultramicroscopy*, vol. 26, no. 1988, pp. 65–69, 1988.

[30]   Gatan, *DigitalMicrograph EELS Analysis User's Guide*. 2003, pp. 3–39.

[31]   P. G. Kotula and M. R. Keenan, "M icroscopy M icroanalysis Application of Multivariate Statistical Analysis to STEM X-ray Spectral Images : Interfacial Analysis in Microelectronics," *Microsc. Microanal.*, pp. 538–544, 2006.

[32]   T. Malis, S. C. Cheng, and R. F. Egerton, "EELS log-ratio technique for specimen-thickness measurement in the TEM.," *J. Electron Microsc. Tech.*, vol. 8, pp. 193–200, 1988.

[33]   E. F. Rauch, J. Portillo, S. Nicolopoulos, D. Bultreys, S. Rouvimov, and P. Moeck, "Automated nanocrystal orientation and phase mapping in the transmission electron

microscope on the basis of precession electron diffraction," *Zeitschrift fur Krist.*, vol. 225, pp. 103–109, 2010.

[34]   A. Kobler, A. Kashiwar, H. Hahn, and C. Kübel, "Combination of in situ straining and ACOM TEM: a novel method for analysis of plastic deformation of nanocrystalline metals.," *Ultramicroscopy*, vol. 128, pp. 68–81, May 2013.

[35]   D. K. Smith and H. W. Newkirk, "The crystal structure of baddeleyite (monoclinic ZrO_2) and its relation to the polymorphism of ZrO_2," *Acta Crystallogr.*, vol. 18, pp. 983–991, 1965.

[36]   X. Mu, "TEM study of the structural evolution of ionic solids from amorphous to polycrystalline phases in the case of alkaline earth difluoride systems: Experimental exploration," *Dissertation*, pp. 31–34, 2013.